Dalton Transactions

ROYAL SOCIETY OF CHEMISTRY

PAPER

View Article Online
View Journal | View Issue

Cite this: *Dalton Trans.*, 2025, **54**, 17662

Tuning the electronic properties of Fe(II)–NHC sensitizers with thienyl π-extended ligands

Nour Shalhoub,[a] Edoardo Marchini, *[b] Federico Coppola, [c,d] Roberto Argazzi,[e] Stefano Caramori, [b] Mariachiara Pastore, *[c] Philippe Pierrat [a] and Philippe C. Gros *[a,f]

Received 26th September 2025,
Accepted 10th November 2025

DOI: 10.1039/d5dt02301g

rsc.li/dalton

Heteroleptic Fe(II)–NHC sensitizers **NS158**, **NS271** and **NS252** bearing fused thiophenes and carboxylic or thienylcyanoacrylic anchoring moieties were designed to enhance light harvesting *via* HOMO inversion in DSSCs. The complexes were comprehensively characterized in solution and when immobilized on TiO_2 photoanodes using electrochemical measurements, transient absorption spectroscopy, and *ab initio* calculations. All tested DSSC samples from these sensitizers exhibited a power conversion efficiency of at least 1% on 18 μm photoanodes. The **NS252** sensitizer combining a thienylcyanoacrylic anchor and a fused dithienyl moiety, showed the broadest absorption up to 750 nm but the lowest IPCE (25%) with 1.07% PCE and a photocurrent of 4.8 mA cm^{-2}. **NS158** and **NS271** bearing respectively a dithienyl and terthienyl fused moiety associated to a carboxylic anchor delivered respectively 1.32% and 0.93% PCE and 5.75 and 4.67 mA cm^{-2} photocurrents. The best efficiency (1.5%) and photocurrent (6.46 mA cm^{-2}) were obtained with **ARM15**, fitted with a single thiophene. The increased conjugation, while enhancing the panchromaticity, reduced dramatically the excited-state directionality, localizing charge away from the anchoring units leading to a lowered coupling for injection into TiO_2. This work highlights the delicate balance to be found between light-harvesting ability, excited-state lifetime, and interfacial charge-transfer efficiency in the design of Fe(II)-based DSSC sensitizers.

Introduction

Replacing noble and rare metals in photoactive materials, core components of solar energy conversion or photocatalysis technologies, is currently an extremely active area of research.[1–4] In this context, iron, the most abundant metal in the earth's crust, has emerged as a promising candidate to replace the ruthenium gold standard.[5–8] However, Fe(II) complexes suffer from short-lived metal to ligand charge transfer (MLCT) states due to ultrafast relaxation to metal centred (MC) states, followed by rapid ground-state recovery thus precluding their successful use in photochemical applications requiring long-lived MLCT states. Thanks to ligands based on σ-donating N-heterocyclic carbene (NHC) units, the MLCT lifetime of iron complexes has been extended up to tens of picoseconds for complexes incorporating C^N^C[9–11] and C^N ligands.[12–14] This has opened the possibility for a series of heteroleptic iron(II) complexes to be effectively used in photochemical applications, such as iron-sensitized solar cells (FeSSCs).[15–22] However, this improvement in lifetime has come at the expense of the panchromatic absorption, that is required for solar energy conversion applications. Recently, the "HOMO inversion" concept has emerged in this field.[23–25] The strategy involves the exploitation of specifically designed ligands having highly π conjugated character, to promote a balanced mixing between metal and ligand molecular orbitals, ideally shifting the HOMO localization from being predominantly metal-based to primarily ligand-based. The use of extended aromatic ligands capable of inducing such delocalized nature of the HOMO has been also predicted to improve light harvesting capabilities, by giving rise to a quite broadened and extended absorption in the visible.[23]

Recently, our group designed a series of Fe(II) homoleptic complexes bearing pyridylNHC ligands extended with fused thiophenes of variable number.[26] In agreement with theoretical projections by the Jakubikova group,[23] these ligands promoted a significant mixture of occupied t_{2g} and ligand π occupied orbitals. This was evidenced by a 80 nm red-shift of the ^{1}MLCT transition, a 2–3-fold increase of the molar extinction coefficient and a doubled MLCT lifetimes (up to 18 ps) com-

[a]*Université de Lorraine, CNRS, L2CM, F-54000 Nancy, France*
[b]*Department of Chemical and Pharmaceutical Sciences, University of Ferrara, Via L. Borsari 46, 44121 Ferrara, Italy*
[c]*Université de Lorraine, CNRS, LPCT, F-54000 Nancy, France*
[d]*Scuola Superiore Meridionale, Largo San Marcellino 10, I-80138 Napoli, Italy*
[e]*CNR-ISOF c/o Department of Chemical, Pharmaceutical and Agricultural Sciences, University of Ferrara, Via L. Borsari 46, 44121 Ferrara, Italy*
[f]*Université de Grenoble Alpes, CNRS, DCM, 38000 Grenoble, France*

pared with a complex deprived of the thiophene moieties.[26] To our knowledge, the impact of such promising ancillary ligands in heteroleptic complexes on the photovoltaic properties of the corresponding device has not been investigated yet. To this purpose, here, we present a series of newly prepared iron(II) complexes bearing fused thiophene units (see Fig. 1 and Fig. S1) and their evaluation as sensitizers in FeSSCs. The photophysical, electrochemical and photovoltaic properties of the new complexes have been investigated in detail. The best efficiency of 1.5% was, however, obtained with **ARM15**, which features a single thiophene unit. While further extending the π-system with additional fused thiophene moieties significantly enhanced the panchromatic absorption, it proved detrimental to excited-state directionality, thereby reducing the effective charge transfer to the anchoring ligand and thus the electron injection capabilities.

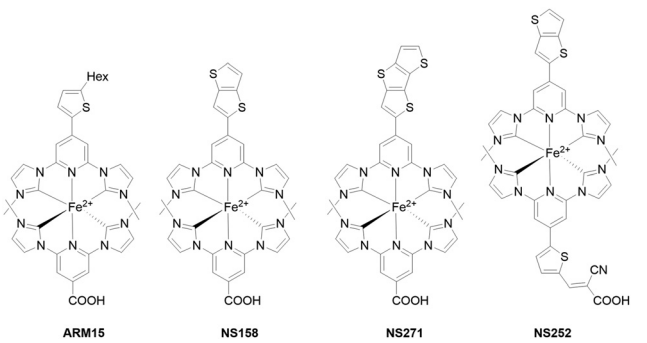

Fig. 1 Complexes studied in this work, the counterion is PF_6^- throughout.

Results and discussion

Synthesis of ligands and complexes

ARM15 was prepared from ref. 20. The synthesis of the target complexes first required the pyridylimidazolium salts **HL1**,[26] **HL2**,[26] **HL3**[27] and **HL4**[21] as precursors of the pyridyl–NHC ligands to be coordinated to iron (Scheme 1). With the precursors in hand, heteroleptic complexes were prepared by combining the appropriate preligands using a statistical methodology consisting of reacting $FeCl_2$ with an equimolar mixture of preligands, ending with the addition of *t*-BuOK or KHMDS as a base to generate the NHC and then coordinate it *in situ*.[16] KHMDS was found to be more efficient than *t*-BuOK in case of **NS252**. The complexes were further cleanly separated by column chromatography from a mixture containing both the homoleptic complexes coming from each ligand concomitantly formed during the process.

Spectroscopic properties of complexes

The UV-Vis spectra recorded in acetonitrile are shown in Fig. 2 and the corresponding absorption maxima gathered in Table 1.

Comparing **ARM15**, **NS158** and **NS271**, clearly showed a slight bathochromic effect on both the π–π* and the lowest MLCT band with a red-shift of about 0.1 eV going from **ARM15**

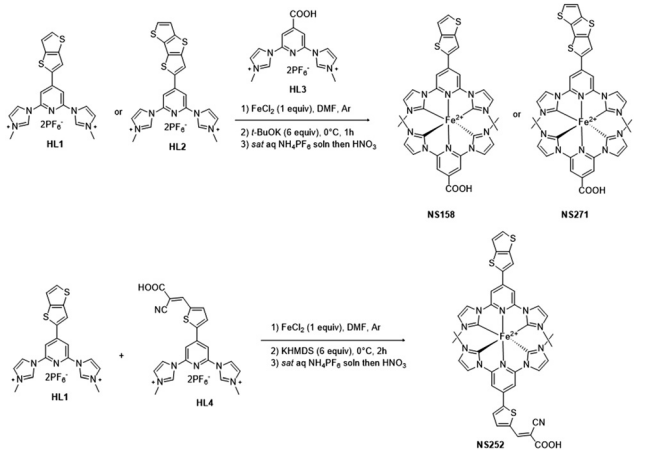

Scheme 1 Synthesis of the complexes studied in this work.

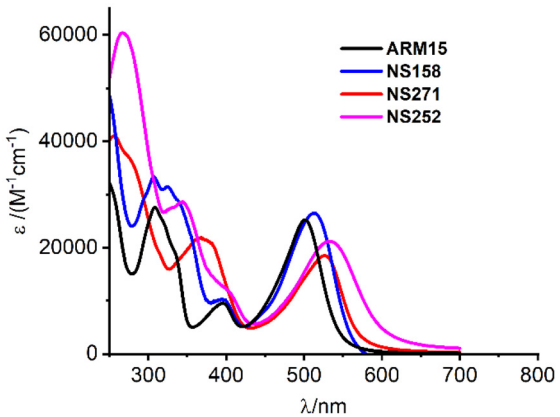

Fig. 2 UV-VIS spectra of the complexes in acetonitrile.

Table 1 Experimental absorption maxima (in CH_3CN and on TiO_2) and calculated vertical excitation energies of the complexes (in CH_3CN). Light harvesting efficiency at λ_{max} on TiO_2 is also reported. See SI for the excited states characterization

	Experiments		Theory
Dye	λ_{max} (nm)-CH_3CN (ε 10^4 (M^{-1} cm^{-1}))	λ_{max} (nm)-TiO_2 (LHE%)	λ_{max} (nm) CH_3CN
ARM15	501 (2.52)	505 (99.6)	458
NS158	513 (2.65)	515 (99.9)	464
NS271	526 (1.85)	525 (99.9)	476
NS252	532 (2.12)	540 (99.9)	520

to **NS271** directly related to the number of thiophene units. The introduction of ThCA (thienocyanoacrylic) in **NS252** expectedly promoted an additional 0.1 eV red shifted (peaking at 532 nm) and a broader absorption compared with **NS158** bearing the carboxylic moiety.

The TD-DFT simulated UV-Vis spectra of all complexes are reported in Fig. 3 and a resume of the low-lying excited states properties is provided in Table S1.

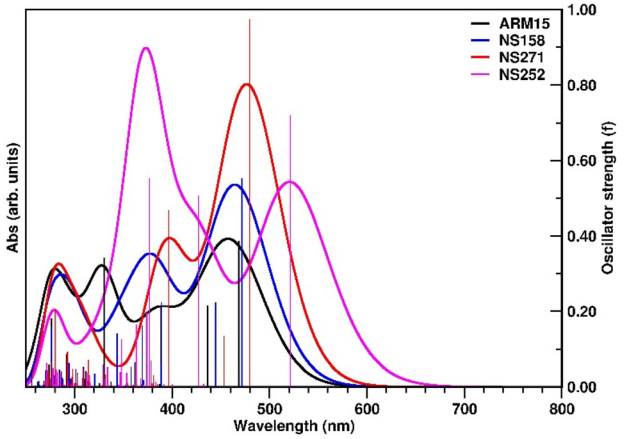

Fig. 3 Simulated absorption spectra of the heteroleptic dyes computed in acetonitrile. A HWHM of 0.20 eV was employed for the gaussian convolution of the vertical excitation energies, reported as vertical sticks.

The spectrum of **ARM15** (Fig. 3) shows a prominent absorption maximum at 458 nm (Table 1), only slightly blue-shifted with respect to the experimental value (501 nm). This band arises from a group of low-lying electronic excitations with dominant MLCT character. The first bright excited state $^1S_4$ at 468 nm, (f = 0.3862) corresponds to a HOMO−2 → LUMO transition, with the *hole* primarily localized on the Fe(II) center and the *electron* density distributed over the anchoring arm – mainly the pyridine and the COOH moieties (see Fig. S2 and NTOs in Fig. S3) – confirming its MLCT nature. The second lower-intensity transition $^1S_6$ (436 nm, f = 0.2144) also exhibits MLCT character, though in this case the *hole* is more localized on the anchoring moiety bearing the carboxylic acid group, while the *electron* density shifts toward the pyridine and –COOH, with a significant contribution on the thiophene-substituted ligand arm. For the transition $^1S_9$ at 388 nm (HOMO → LUMO+3, f = 0.2101), the *hole* remains on the Fe center but with increased contribution from the adjacent NHC ligand backbone and the pyridine linker. The *electron* density is more delocalized on both the NHC–pyridine ligands.

In the case of **NS158**, TD-DFT calculations predict an absorption maximum at 464 nm, closely matching the experimental value (513 nm, Fig. 3). This band is composed of two low-energy electronic excitations. The most intense is $^1S_4$ (472 nm, f = 0.5522), which originates from a HOMO−2 → LUMO transition. NTOs analysis indicate a dominant MLCT character, with the *h–e* pair localized on the same side of the molecule – specifically on the ligand bearing the anchoring group. The second relevant transition $^1S_6$ (445 nm, f = 0.2233) is mainly assigned to a HOMO−1 → LUMO+1 excitation. Here, the primary *h–e* pair (62%) is localized on the ligand containing the fused thiophene rings, while a minor contribution (28%) involved a more delocalized charge distribution spanning both ligands. The electronic excitation leading to the $^1S_{10}$ at 389 nm is moderately bright, f = 0.2230, and see the *hole* primarily localized on the Fe center and, to a lesser extent, on both the core of the NHC-type ligands, while the *electron* involves the pyridine group of the anchoring arm. A more concise analysis is also given in SI (Fig. S4 and S5). The increased electronic conjugation in **NS271** lowers the absorption maximum at 476 nm, with a computed 0.1 eV red shift with respect to **ARM15**, in agreement with the measured bathochromic shift. The most intense contribution corresponds to the $^1S_4$ at 479 nm (f = 0.9723) arising from a combination of HOMO−2 → LUMO (46%) and HOMO−1 → LUMO+1 (48%) transitions. NTO analysis reveals the involvement of two dominant *h–e* pairs one associated with charge transfer toward the NHC–pyridine ligand bearing the anchoring group, and the other directing the electron toward the fused-thiophene moiety. The second transition $^1S_6$ (453 nm, f = 0.1339), is less intense but still exhibits predominant MLCT nature. In this case, an increased ligand-centred (LC) and ILCT component is observed, indicating partial delocalization over the extended thiophene moiety, as also supported by the NTO analysis in Fig. S6 and S7 in SI. The $^1S_{10}$ excited state (397 nm, f = 0.4660) displays a significantly delocalized character. The excitation arises from a hole that is distributed across multiple fragments: while the Fe centre still contributes appreciably, the largest portion of the *hole* density is found on the extended π-system of the substituted ligand, specifically on the fused thiophene unit. The *electron*, on the other hand, is primarily localized on the pyridine fragment and on the fused thiophene, with a minor but notable contribution from the lateral NHC units. These *h–e* distributions suggest a pronounced ligand-centred nature in addition to the MLCT contribution that characterized this excited state. The **NS252** complex is structurally analogous to **NS158**, but features a functionalized anchoring arm, bearing the ThCA group. This modification extends the π-conjugation and increases the charge-transfer nature of the low-lying excited states, see Fig. S8. To alleviate the underestimation of the excitation energies due to the higher degree of CT, for this complex, we employed the B3LYP functional, incorporating an higher fraction (20%) of Hartree–Fock exchange, in place of the B3LYP* variance (15%).[16] The simulated optical spectrum shows a pronounced redshift of the first absorption band (520 nm) compared to the previous cases, once again in good agreement with the experimental value at 532 nm. The low-energy region of the spectrum is dominated by a single bright transition $^1S_3$ (522 nm, f = 0.7195), corresponding to a purely HOMO−2 → LUMO excitation, as shown in Fig. S9. This state shows a MLCT nature, with both the *hole* and *electron* densities localized on the same ligand arm, specifically the one functionalized with the ThCA anchoring group (see Fig. S9).

The electronic transition $^1S_8$ (at 427 nm, f = 0.5057), displays an overall MLCT character like $^1S_3$, but involves two *h–e* pairs. For the dominant configuration (80%), the density is primarily localized on the ligand bearing the two thiophene rings, whereas the minor component involves both pyridyl–NHC ligands around the metal centre.

The $^1S_{13}$ excited state at 377 nm shows a strong oscillator strength, 0.5507, and involves multiples orbital transitions, see Table S1 in SI. In the dominant pair (69%), the *hole* density is

mainly localized on the ThCA arm and the thiophene ring, with additional contribution from the two fused thiophene rings opposite to the anchoring site, while the *electron* density is entirely localized on ThCA. The second pair (15%) introduces partial ILCT character, as the *h*–*e* density is redistributed between the two orthogonal ligands: the one near the anchoring site and the one bearing the two fused thiophene rings.

As a complementary analysis, we also performed a fragment-based population study (Table S2) on the lowest bright singlet states. The definition of the fragments is provided in Fig. S10. This approach provides a quantitative description of how the *hole* and *electron* densities are partitioned among the different molecular fragments (*i.e.*, the anchoring group and the π-extended units), thereby offering a more detailed picture of the nature of the electronic excitations. Such a decomposition not only corroborates the spectroscopic assignments obtained from orbital analysis but also clarifies the extent to which charge redistribution occurs upon excitation.

Spectroscopic and electrochemical properties of FeNHC-sensitized photoanodes

To gain information about the spectroscopic features of the new complex series on TiO_2, 12 μm thick dye-sensitized electrodes have been prepared. Their relative absorption spectra are depicted in Fig. 4 and λ_{max} values reported in Table 1.

The chemisorbed dyes exhibited an intense symmetric CT band, covering the 425–600 nm region. **NS252** exhibits the broadest and most red-shifted band extended up to 700 nm, in agreement with its spectrum in solution. The relatively narrow CT bands exhibited by the entire Fe(II)–NHC family ensure efficient absorption of incident photons at the λ_{max} (from 99.6% to 99.9%), although this absorption rapidly falls off in the lower energy region of the visible spectrum. To improve light harvesting capability, we increased the TiO_2 thickness to 18 μm and applied a top scattering layer composed of particles larger than 100 nm. With this electrode configuration, the absorption profiles became broader and more intense, saturating the photometric response of our apparatus (Fig. 4b). Notably, the spectral response was sizably extended to 650 nm for the dye bearing a single thiophene unit (**ARM15**), and up to 750 nm for the complex with two fused organic molecules and the ThCA anchoring group (**NS252**). Since **NS252** exhibits a "valley" at 500 nm, we designed two different co-sensitization strategies to achieve panchromatic absorption and cover both the high (450–550 nm) and low energy (550–650 nm) regions. In the first attempt, **NS252** was combined with **ARM15**, and in the second with **NS158**. Fig. 4b clearly supports the presence of these components chemisorbed at the TiO_2 surface, with a sharp maximum around 500 nm consistent with the fingerprint of –COOH-based dyes, followed by a lower energy shoulder attributable to the ThCA-bearing Fe(II)NHC complex.

The FTIR-ATR spectra of the sensitized TiO_2 (Fig. S12) clearly confirm the interaction of the complexes with the TiO_2. The spectra exhibit broad bands at 1624 cm^{-1} assigned to the asymmetric stretching vibration of the carboxylate groups, confirming the attachment of the sensitizers to the semiconductor

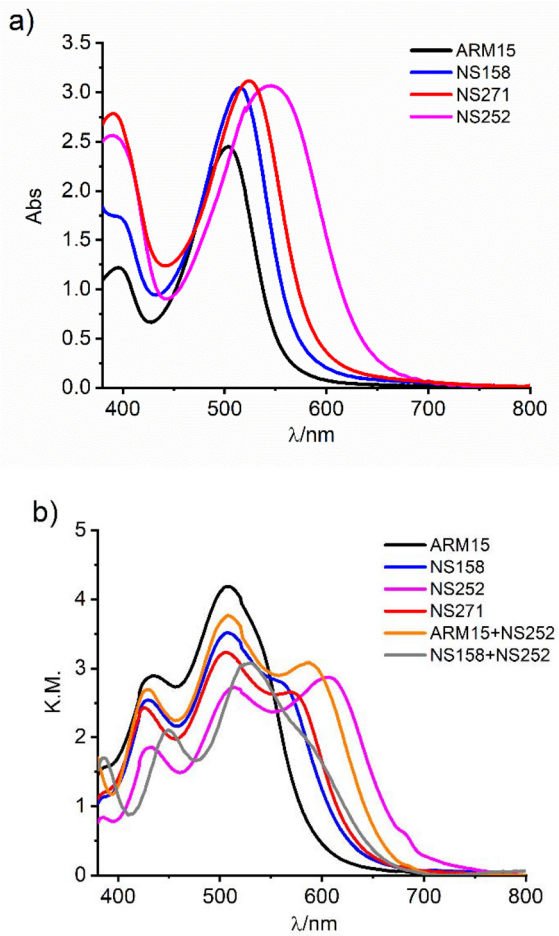

Fig. 4 Absorption of the complexes on (a) 12 μm and (b) 18 μm TiO_2 electrodes. Spectra recorded against an identical undyed TiO_2 electrode as reference.

surface mostly *via* coordination of the COO^- group to Ti(IV) centres. The COO^- coordinated to the Ti(IV) sites also results in a band at 1346 cm^{-1}.[15]

Cyclic voltammetry was then performed on the sensitized TiO_2 or ZrO_2 thin films in contact with 0.1 M $LiClO_4$/acetonitrile solution (Fig. 5 and Table 2). ZrO_2 is known as a porous, electrochemically inert support that can be used to explore the energetics of dyes' reduction[28–30] that is precluded on TiO_2 due to interception of the CB states. In both cases the oxidative response is mediated by the fraction of complexes electronically coupled with FTO, triggering a cascade of electron transfer events *via* surface hopping involving adjacent redox centres. This makes the observation of a clear electrochemical response feasible even at potentials where both these n-type semiconductors exhibit an insulating behaviour.

The Fe(II)/Fe(III) redox process of the dyes grafted on TiO_2 is, in the whole series, quasi-reversible ($\Delta E \approx 80$ mV), centred at *ca.* 0.62/0.61 V *vs.* SCE. Notably, this faradaic process remains unaffected by the increased π-conjugation resulting from the progressive fusion of thiophene unites (Fig. 5a). Analogously, all complexes exhibit similar reversible oxidation behaviour

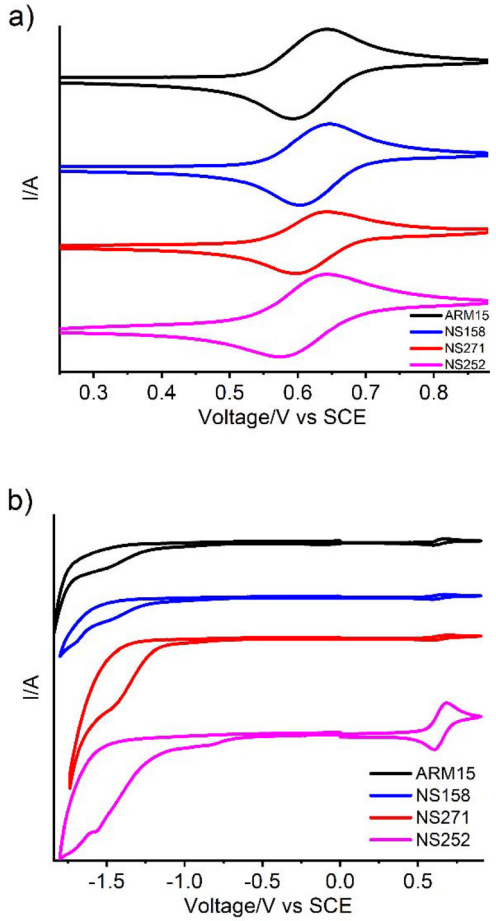

Fig. 5 Cyclic voltammetry recorded for the complexes on (a) TiO_2 and on (b) ZrO_2 (full scan) in 0.1 M $LiClO_4$/ACN solution.

when anchored on ZrO_2. On the cathodic side (Fig. 5b), an irreversible multi-electronic reduction wave is observed for the whole series. The LUMO is progressively stabilized from **ARM15** (−1.49 V *vs.* SCE) to **NS271** (−1.46 V *vs.* SCE). Consistent with our previous findings, the functionalization with the ThCA anchoring moieties in **NS252** results in a broadened reduction process, indicative of a distribution of redox sites introduced by the cyano-acrylic group, with a first peak at −0.83 V *vs.* SCE, which is absent in the –COOH-based dyes. The red shifted MLCT bands observed going from **ARM15** to **NS252** agree with the decreasing electrochemical gap (Table 2) and the calculated HOMO–LUMO gap, as shown in Fig. S10. Thus, the stabilization of the LUMOs, which are primarily localized on the π*-ligands orbitals, is responsible for a significant red shift in the spectra response of **NS158**, **NS271** and **NS252** compared to **ARM15**. Such stabilization is also expected to influence the t_{2g} metal orbitals (Fig. S13a), leading to a concomitant stabilization of the HOMOs.

However, the entire iron series displayed nearly identical oxidation potentials (Table 2) nicely correlating with the extremely close Khon–Sham eigenvalues calculated for the HOMOs (Fig. S11), suggesting a concurrent destabilization of the filled π-orbitals of the ligands, which counteracts the expected anodic shift of the Fe(II)/Fe(III) oxidation (Fig. S13b) with increased π donation by the ligand orbitals. As a matter of fact, the calculated percentage of Mulliken population localized on the HOMOs is almost constant within the series and amount to about 60% (Fig. S11). A schematic representation of the energetic of the HOMO and LUMO levels is depicted in Fig. 6.

Since as expected,[9] the iron(II) complexes were not emissive in solution nor loaded on the semiconductor, the zero–zero excitation energy E^{oo} was estimated from the onset of the absorption spectra at *ca.* 5% of the maximum absorption. E^{oo} decreased significantly following the order **ARM15** (2.07 eV) > **NS158** (2.03 eV) > **NS271** (1.97 eV) > **NS252** (1.81 eV). These

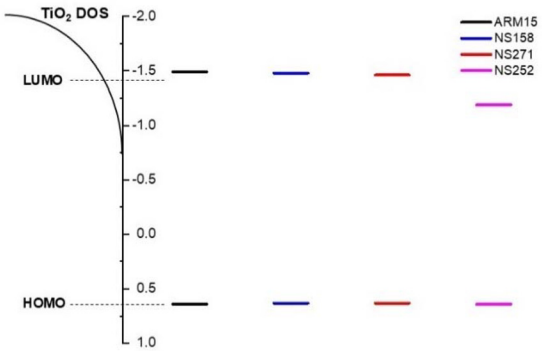

Fig. 6 Representation of the frontier interfacial energy levels of the Fe (II) sensitizers obtained from the electrochemical study.

Table 2 Electrochemical and spectroscopic parameters for the Fe(II)NHC sensitized TiO_2 and ZrO_2

Dye	E_{ox} (TiO_2) (V *vs.* SCE)	E_{ox} (ZrO_2) (V *vs.* SCE)	$E_{(peak)red}$ (ZrO_2) (V *vs.* SCE)	ΔE_{redox} [a] (ZrO_2) (eV)	E^{oo} [b] (TiO_2) (eV)	E^{*}_{ox} [c] (TiO_2) (V *vs.* SCE)
ARM15	0.62	0.64	−1.49	2.13	2.07	−1.45
NS158	0.62	0.63	−1.48	2.11	2.03	−1.41
NS271	0.61	0.63	−1.46	2.09	1.97	−1.36
NS252	0.61	0.64	−0.83 −1.54	1.83[d]	1.81	−1.20

[a] Calculated according to: $|E_{ox}(ZrO_2)| + |E_{red}(ZrO_2)|$. [b] The $E^{oo}_{(TiO_2)}$ energy was estimated from the onset of the absorption spectrum, by taking the 5% absorbance relative to the MLCT maximum on TiO_2. [c] Calculated according to: $E_{ox}(TiO_2) - E^{oo}_{Abs\text{-}TiO_2}$. [d] Due to the broad reduction wave, an average potential value of −1.19 ((−0.83–1.54)/2) was considered.[21]

estimated values agree with the electrochemical gaps. The excited state oxidation potential $E^*_{ox}\left(E^*_{ox} = E_{ox} - E^{oo}\right)$ logically decreased going from **ARM15** to **NS252** where the lowest value was obtained (−1.2 eV).

The driving force of injection in the TiO_2 semiconductor can be calculated according to $\Delta G_{inj} = -e\left(|E^*_{ox}| - |E_{FB}|\right)$ where E_{FB} represents the flat band potential of the TiO_2 accepted to lay at *ca.* −0.7 V *vs.* SCE in an organic medium in the presence of intercalating lithium cations.[31] ΔG_{inj} values were found in the 500–750 meV range securing an exergonic injection process in the TiO_2 semiconductor. The ground state oxidation potentials are also in favour of an exergonic regeneration process (at least 200 mV) of the Fe(II) species by the iodide/triiodide-based electrolyte.

Transient absorption spectroscopy

Regeneration and recombination dynamics on TiO_2 were investigated by means of transient absorption spectroscopy (TAS) in the μs–ms timescale for the entire series. The difference spectra evaluated for the Fe(II)–NHC family in contact with 0.1 M $LiClO_4$/acetonitrile solution exhibited common features in the whole series (Fig. S14). The 532 nm excitation resulted in an intense ground state bleach centred around 500 nm, formed within the instrumental response of our spectrometer (FWHM = 100 ns, R = 350 Ω). This fingerprint closely mirrors the MLCT manifold once the small bathochromic shift of the ground state, accounting for the intercalation of small cations such as Li^+ and Mg^{2+}, is considered.[16] In accordance with its ground state absorption spectrum, **NS252** displayed the broadest and most extended bleaching across the series (Fig. S14d). The TA spectra also revealed a high-energy absorption around 430 nm and a low-energy flat absorption above 650 nm, both attributable to LMCT transitions. At lower energies (λ > 750 nm), electrons trapped in TiO_2 further contribute to this featureless absorption band. The TA spectra of the co-sensitized systems (**ARM15** + **NS252** and **NS158** + **NS252**) revealed contributions from both sensitizers, confirming the ability of each component of cocktail to inject independently from the other: in particular, the intense 500 nm bleach of **ARM15** and **NS158** is followed by the red shifted fingerprint of **NS252** (Fig. S14e and S14f).

Since only ≈50% of the decay was recovered within the explored time window, recombination dynamics were further analysed by monitoring the 500 (for **ARM15**, **NS158** and **NS271**) or 550 nm (**NS252**) kinetics extending the timescale to 500 ms (Fig. 7). The excitation power was reduced to 400 μJ per cm^2 per pulse to prevent the generation of excess electron–hole pairs, which would artificially accelerate recombination events. To optimize the signal-to-noise ratio (S/N), oscillographic traces were pre-amplified using input impedances of either 10 kΩ or 1 MΩ. The recovery of the photoinduced bleach of dyed TiO_2 in contact with a I^-/I_3^- free electrolyte (0.1 M LiOTf, 0.6 M PMIOTf, 0.1 M GuNCS, 0.1 M $TBAPF_6$, 0.1 M $Mg(OTf)_2$) is shown in Fig. 7a. The recombination kinetics were fitted using a combination of a power law function (eqn (1a)), describing fast bimolecular electron–hole recombination

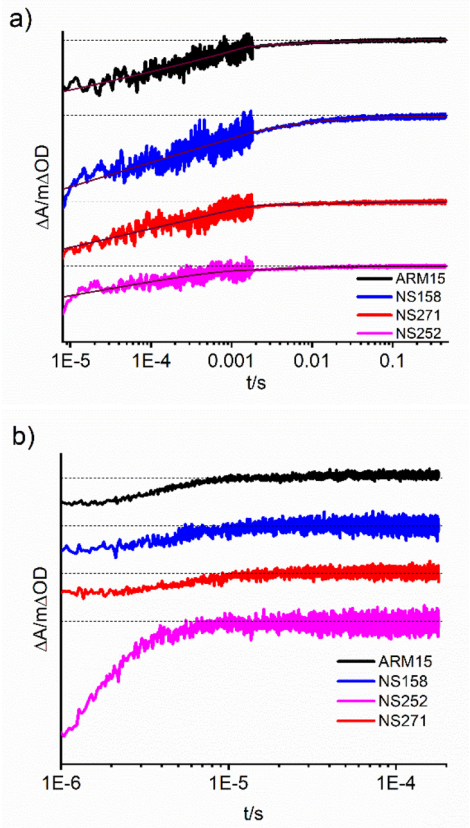

Fig. 7 (a) Recombination dynamics of the Fe(II)-complexes supported on TiO_2 in contact with an electrolyte deprived of the I^-/I_3^- redox couple (0.1 M LiOTf, 0.6 M PMIOTf, 0.1 M GuNCS, 0.1 M $TBAPF_6$, 0.1 M MgOTf). The decays were recorded at 500 nm except for **NS252** that was evaluated at 550 nm. The excitation energy was 400 μJ per cm^2 per pulse. The kinetics were obtained by joining traces recorded with 10 kΩ and 1 MΩ. (b) Regeneration dynamics of the electrodes reported in (a) in contact with the reduced form of the electrolyte (I^-). Input impedance: 10 kΩ.

that accounts for *ca.* 60% of the initial amplitude recovery at early times (t < 2 ms), and a stretched exponential (Kohlraush–Williams–Watts (KWW)) function for t > 2 ms (eqn (1b)). The latter models the intrinsic heterogeneity of the nanocrystalline of the surface, which gives rise to a distribution of rate constants due to electron trapping/detrapping in localized states close to the conduction band edge of the semiconductor.

$$\Delta A_{t<2\ ms} = A + bt^{-c} \quad (1a)$$

$$\Delta A_{t>2\ ms} = A' + b'e^{\left(\frac{t}{\tau_0}\right)^{\beta}} \quad (1b)$$

β in eqn (1b) is the exponential stretching parameter, set to 0.25 for all decays.[32] Weighted lifetimes were computed from τ_0 according to:

$$\langle\tau\rangle = \frac{\tau_0}{\beta}\Gamma\left(\frac{1}{\beta}\right) \quad (2)$$

where Γ is the gamma function.[33] The $\langle\tau\rangle$ values for the entire series fall within the ms range (Table 3), spanning from 3.2 for

NS158 to 14.3 ms for **NS271**. The longer lifetime of **NS271** is probably consistent with less efficient electron injection which yields to a lower concentration of electron/hole pairs.

For the co-sensitized systems (**ARM15** + **NS252** and **NS158** + **NS252**), recombination kinetics were probed at both 500 and 550 nm (Fig. S15). At higher energies, the dominant spectral contributions arise from **ARM15** and **NS158**, while at longer wavelengths **NS252** prevails. The shorter $\langle\tau\rangle$ values obtained at 500 nm for **ARM15** and **NS158** compared to their individual lifetimes suggests the possibility of partial hole transfer from **ARM15** and **NS158** to that fraction of **NS252** which remained at the reduced state, being unable to inject (Table S3). This is consistent with the slightly cathodic oxidation potential of the latter and with injection quantum yields that are <1. Under no circumstances are the small differences in recombination lifetime detrimental to DSSCs operation. Indeed, upon introducing iodide into the electrolyte (without I_2), the Fe(III) bleach recovery for the entire Fe(II)–NHC series is largely confined within the instrumental response of our spectrophotometer (10 kΩ input impedance) (Fig. 7b and S16). This indicates nearly quantitative regeneration efficiency (η_{reg}), expressed by eqn (3):

$$\eta_{reg} = \frac{k_{reg}}{k_{reg} + k_{rec}} \quad (3)$$

where k_{reg} is the pseudo first order rate constant associated with the regeneration of the Fe(II) species by the reduced form of the redox mediator on the order of 10^6 s^{-1}, and the k_{rec} represents the recombination rate constant on the order of 10^3 s^{-1}. Since k_{reg} is at least three orders of magnitude larger than k_{rec}, $\eta_{reg} \approx 1$ can be safely concluded.

Photovoltaic properties

The photovoltaic properties of this new Fe(II)–NHC series were investigated by means of photoaction spectra and photocurrent densities/voltage (*JV*) measurements (Fig. 8).

The studies were performed in the presence of our additive-rich electrolyte in which the I^-/I_3^- mixture contains intercalating cations such as Li^+ and Mg^{2+}, which contribute to downshift the TiO_2 Fermi level and enhance excited state directionality though the generation of a favourable surface dipole that promotes higher electronic coupling and improves charge injection.[16,21] In addition, GuNCS was introduced to partially shield the titania surface from recombination of photoinjected electrons with I_3^-. However, as it is not capable of shifting the Fermi Level, only a modest improvement in V_{oc} was observed.

Table 3 Recombination lifetime for the Fe(II)–NHC complexes obtained from eqn (1a), (1b) and (2)

Dye	τ_0/s	$\langle\tau\rangle$/ms
ARM15	2.88×10^{-4}	6.9
NS158	1.35×10^{-4}	3.2
NS271	5.97×10^{-4}	14.3
NS252	2.71×10^{-4}	6.5

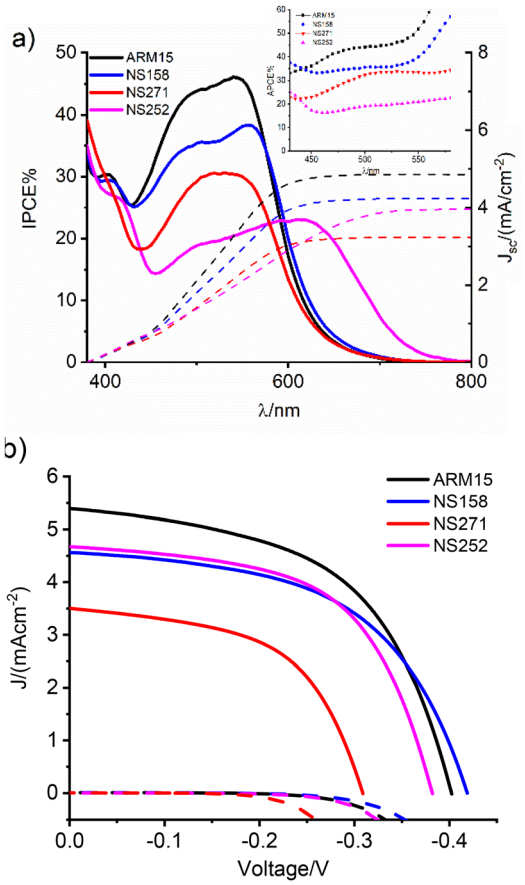

Fig. 8 (a) IPCE spectra for the Fe(II)-based complexes and integrated photocurrent from the IPCE plots. (b) *JV* curves for the dyed 12 μm TiO_2 electrodes.

On transparent thin films (12 μm thick TiO_2), the Fe(II)–NHC series displayed Incident-Photon-to-Current-Conversion Efficiency (IPCE) spectra that decreased with increasing ligand conjugation, arising from fused thiophene units, from 50% for **ARM15** (1 thiophene) to 30% for **NS271** (three fused thiophenes) (Fig. 8a). Within the series, **NS252** exhibited the lowest IPCE (25%) but the broadest spectral extension, consistent with the pronounced bathochromic shift induced by the ThCA anchoring group, which further stabilizes the LUMO, allowing the complex to collect and convert photons up to 750 nm. The computed Absorbed-Photon-to-Current-Conversion Efficiency (APCE) spectra confirmed the decrease in charge injection, with values following the order **ARM15** (45%) > **NS158** (40%) > **NS271** (30%) > **NS252** (20%) (Fig. 8a – inset). Under AM1.5G illumination, the progressive bathochromic shift associated with LUMO stabilisation proved insufficient to compensate for the decline in injection. Accordingly, *JV* measurements (Fig. 8b) revealed the highest photocurrent density of 5.4 mA cm^{-2} for **ARM15** and the lowest of 3.5 mA cm^{-2} for **NS271**. **NS158** and **NS252** delivered essentially the same photocurrent, the former benefiting from higher injection and the latter from broader spectral sensitivity. The photocurrent density measured under full spectrum is consist-

Table 4 Photovoltaic parameters for the Fe(II)–NHC family on 12 μm thick TiO_2

Dye	J_{sc}/(mA cm^{-2})	V_{oc}/V	FF%	η%
ARM15	5.39 ± 0.14	0.40 ± 0.01	54 ± 2	1.16 ± 0.03
NS158	4.56 ± 0.20	0.42 ± 0.01	54 ± 1	1.02 ± 0.04
NS271	3.51 ± 0.10	0.31 ± 0.01	54 ± 1	0.59 ± 0.03
NS252	4.68 ± 0.12	0.38 ± 0.01	57 ± 1	1.02 ± 0.04

ent with the integrated IPCE plots in Fig. 8a. The corresponding Power conversion Efficiencies (PCEs, Table 4) followed the order 1.16% (**ARM15**) > 1.02% (**NS158** and **NS252**) > 0.59% (**NS271**) (Table 4). The drop in injection across the series cannot be attributed solely to the small decrease in injection driving force, since the variation in E^*_{ox} going from **ARM15** to **NS271** was only 30 mV. Inspection of the computed NTOs for the lowest-energy excited states (Fig. S3, S5, S7 and S8) and the corresponding analysis of the *hole* and *electron* localization over the different molecular fragments (Table S2 and Fig. S10), well rationalise the measured photocurrents and injection efficiencies. As the number of thiophene units increases in the series, going from **ARM15** to **NS271**, the efficiency of the charge transfer toward the anchoring group decreases, as is apparent from the increasing weight in the lowest bright state of the NTOs pair moving charge toward the ancillary ligand. If the electron localized on the COOH anchoring moiety is taken as a rough estimation of the capability of injecting charge into the TiO_2 CB, this value decreases within the series: 0.15 (**ARM15**), 0.13 (**NS158**) and 0.09 for **NS271** (Table S2). The increase in conjugation on the ancillary ligand appears, thus, detrimental to the excited state directionality, progressively localizing the photoexcited electron on the fused thiophenes, that are spatially opposite to the anchoring units and hence decoupled from the titania surface. As far as **NS252** is concerned, the calculated *hole*/*electron* localization and the NTOs indicate, on the other hand, an optimal excited-state topology for charge injection into the semiconductor (Table S2 and Fig. S8). The lower IPCE and photocurrent values, compared to **ARM15**, can thus be attributed to inefficient electronic coupling between the dye's LUMO and the CB acceptor states. This inefficiency may arise from an unfavourable adsorption configuration and the consequent disruption of electronic conjugation, a phenomenon already reported by some of us for an analogous ThCA-bearing Fe(II)–NHC complex.[21]

When DSSCs were assembled with the thicker TiO_2 (18 μm) coupled with a top scattering layer, their broader spectral extension (see IPCEs and the associated integrated photocurrents in Fig. S17) significantly enhanced the photocurrent (6.46 mA cm^{-2} for **ARM15** and 5.75 mA cm^{-2} for **NS158**, Fig. 9), particularly for dyes absorbing in the high energy region of the solar spectrum. Consequently, the PCEs increased following the order 1.50% (**ARM15**) > 1.32% (**NS158**) > 1.07% (**NS252**) > 0.93% (**NS271**) (Table 5). The panchromatic response obtained by co-sensitizing blue and red absorbing

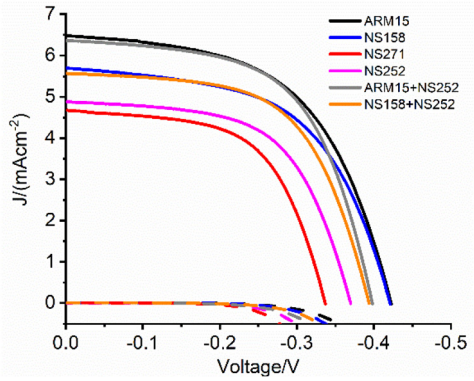

Fig. 9 *JV* curves for the dyed 18 μm + scattering layer TiO_2 electrodes.

Table 5 Photovoltaic parameters for the Fe(II)–NHC family on 18 μm thick TiO_2 + scattering layer

Dye	J_{sc}/(mA cm^{-2})	V_{oc}/V	FF%	η%
ARM15	6.46 ± 0.22	0.42 ± 0.01	55 ± 1	1.50 ± 0.09
NS158	5.75 ± 0.13	0.42 ± 0.01	55 ± 1	1.32 ± 0.06
NS271	4.67 ± 0.31	0.34 ± 0.02	59 ± 3	0.93 ± 0.06
NS252	4.88 ± 0.21	0.37 ± 0.01	59 ± 1	1.07 ± 0.02
ARM15 + **NS252**	6.36 ± 0.11	0.40 ± 0.01	59 ± 1	1.49 ± 0.08
NS158 + **NS252**	5.57 ± 0.48	0.39 ± 0.01	60 ± 2	1.30 ± 0.05

dyes (**ARM15** + **NS252** and **NS158** + **NS252**) was confirmed by IPCE spectra, which showed spectral contributions from both species, confirming the TAS data, with a first broad band ranging from 500 to 600 nm and a shoulder between 600 to 750 nm, indicating that both dyes are capable of harvesting visible photons and injecting electrons into the semiconductor. However, the coexistence of both species did not yield further improvements in photocurrent (6.36 mA cm^{-2} for **ARM15** + **NS252** and 5.57 mA cm^{-2} for **NS158** + **NS252**), suggesting that the reduced loading of the former dye, more efficient, resulted in a loss of harvesting and injection, which was not compensated by the extended spectral response of the co-sensitized electrode. Thus, the best performing co-sensitized device achieved the same efficiency as **ARM15** alone (1.5%, Table 5).

In view of gaining insight into the key factors controlling the performance of the devices, the photocurrent values for the entire series were plotted against their V_{oc}. According to the diode equation,[34] Fig. S18a shows a linear dependency of the V_{oc} on lnJ_{sc}, indicating that the photocurrent generated by the Fe(II)–NHC complexes (Fig. 9) is mainly controlled by charge injection. Possible deviations from linearity could occur when the net photocurrent is also influenced by recombination events between the photoinjected electrons and the oxidized form of the electrolyte (I_3^-) occurring with different rate constants. However, Tafel plots computed from dark current curves (Fig. S18b) revealed similar slopes for the entire series, confirming similar recombination kinetics. Since the dark current is controlled by recombination with I_3^-, the Tafel

analysis also allowed to extract the exchange current density (i_0) related to electron transfer to the I_3^-, yielding values on the order of 10^{-7} A cm^{-2} for the entire series, consistent with the range of values typically reported for DSSC based on the I^-/I_3^- couple.[35] Considering the Butler–Volmer equation,[36] these values led us to estimate an electron transfer rate constant (K_{et}) on the order of 10^{-9} cm^{-1}. This confirms that, in the present case, the cell performances are mainly dictated by charge injection yields rather than by different rates of recombination events occurring with the redox couple at the dyed TiO_2/electrolyte interface.

Experimental section

Solvents were purified by standard procedures and purged with argon before use. All other chemicals used in this work were of analytical grade and were used without further purification until or unless stated, and all reactions were performed under an inert atmosphere of argon. Chromatographic separations were carried out on silica gel (60–120 mesh). ^{1}H (400 MHz) and ^{13}C NMR (100 MHz) spectra were taken on a DRX400 Bruker spectrometer at ambient temperature. High-resolution mass spectrometry (HRMS) data was obtained by using Bruker micrOTOF-Q spectrometer. UV-vis spectra were recorded in a 1 cm path length quartz cell on a LAMBDA 1050 (PerkinElmer), spectrophotometer.

Synthesis of complexes

NS158. HL1 (95 mg, 0.142 mmol), **HL3** (80 mg, 0.142 mmol) and $FeCl_2$ (18 mg, 0.142 mmol) were dried under vacuum at 80 °C overnight. After 3 cycles of vacuum/argon, anhydrous DMF (2 ml) was added. 3 cycles of freeze–pump–thaw were performed to degas the reaction mixture and *t*-BuOK was added at once (0.71 mmol, 0.08 g) at room temperature. The color directly changed from yellow to purple upon addition of *t*-BuOK. After 1 h, the reaction was completed (seen by TLC monitoring). The reaction mixture was filtered over Celite and recovered in acetonitrile. After evaporation of acetonitrile, a saturated solution of NH_4PF_6 was added (10 mL), followed by HNO_3 until the solution becomes acidic (pH = 2) and the precipitate was collected by filtration. Then, the crude was purified on silica gel column chromatography using acetone/H_2O/KNO_3 (10/3/0.5). The heteroleptic fraction was collected and after evaporation of acetone, a solution of NH_4PF_6 was added followed by HNO_3 until the solution becomes acidic (pH = 2) affording the precipitation of the desired complex **NS158**. The latter was recovered by filtration, washed with diethyl ether and dried under vacuum. The isolated complex **NS158** was obtained as a pink colored compound (20 mg, 7% yield). ^{1}H NMR (400 MHz, acetonitrile-d_3) δ 8.34 (s, 2H), 8.26 (s, 1H), 8.19 (d, J = 2.2 Hz, 2H), 8.15 (d, J = 2.2 Hz, 2H), 8.05 (s, 2H), 7.73 (d, J = 5.3 Hz, 1H), 7.49 (d, J = 5.3 Hz, 1H), 7.04 (d, J = 2.1 Hz, 2H), 7.02 (d, J = 2.1 Hz, 2H), 2.64 (s, 6H), 2.51 (s, 6H). ^{13}C {^{1}H} NMR (101 MHz, CD_3CN) δ 200.8, 200.6, 155.3, 154.8, 145.5, 142.5, 142.2, 141.4, 132.2, 127.6, 127.5, 121.4, 121.1, 117.7, 117.5, 105.9, 102.4, 35.7, 35.2. ESI-HRMS calcd for $C_{33}H_{28}FeN_{10}O_2S_2$ m/z = 358.0588. Found: 358.0595.

NS271. Applying the above-described procedure to **HL2** (79 mg, 0.142 mmol), **HL3** (100 mg, 0.142 mmol), and $FeCl_2$ (18 mg, 0.142 mmol) afforded **NS271** as a dark pink colored compound (13 mg, 9% yield). ^{1}H NMR (400 MHz, acetonitrile-d_3) δ 8.31 (s, 1H), 8.29 (s, 1H), 8.17 (d, J = 2.2 Hz, 2H), 8.14 (d, J = 2.2 Hz, 2H), 8.05 (s, 2H), 7.69 (d, J = 5.3 Hz, 1H), 7.5 (d, J = 5.3 Hz, 1H), 7.03 (d, J = 2.2 Hz, 2H), 7.02 (d, J = 2.2 Hz, 2H), 2.64 (s, 6H), 2.5 (s, 6H). ^{13}C NMR (101 MHz, CD_3CN) δ 200.6, 200.4, 165.7, 155.5, 154.7, 145.2, 144.9, 143.7, 141.0, 138.7, 133.6, 130.2, 127.7, 122.9, 122.3, 117.7, 117.6, 105.6, 102.4, 35.7, 35.6. ESI-HRMS calcd for $C_{35}H_{28}FeN_{10}O_2S_3$ m/z = 386.0449. Found: 386.0446.

NS252. Applying the above-described procedure to **HL1** (95 mg, 0.142 mmol), **HL4** (100 mg, 0.142 mmol), and $FeCl_2$ (18 mg, 0.142 mmol) and using KHMDS (0.85 mmol, 0.85 mL, 1 M) at 0 °C (instead of *t*-BuOK at room temperature) afforded **NS252** as a violet solid (10 mg, 6% yield). ^{1}H NMR (400 MHz, acetonitrile-d_3) δ 8.52 (s, 1H), 8.25 (s, 1H), 8.18 (d, J = 2.5 Hz, 2H), 8.15 (d, J = 2.5 Hz, 2H), 8.11 (s, 2H), 8.07 (d, J = 4.1 Hz, 1H), 8.05 (s, 2H), 7.99 (m, 1H), 7.14 (d, J = 5 Hz, 1H), 7.50 (d, J = 5 Hz, 1H), 7.04 (m, 4H), 2.63 (s, 6H), 2.58 (s, 6H). ^{13}C NMR (101 MHz, CD_3CN) δ 201.1, 200.9, 155.1, 154.9, 142.6, 142.1, 141.4, 132.2, 132.0, 131.8, 129.2, 127.6, 127.5, 121.3, 121.1, 117.6, 117.5, 102.8, 102.3, 100.4, 99.7, 35.7, 30.9. ESI-HRMS calcd for $C_{40}H_{31}FeN_{11}O_2S_3$ m/z = 424.5582. Found: 424.5580.

DSSC fabrication and characterization

Guanidinium thiocyanate (GuNCS) ≥ 97%, ACS grade I_2 ≥ 99.8%, 99.995% lithium trifluoromethanesulfonate (LiOTf), 97% magnesium trifluoromethanesulfonate ($Mg(OTf)_2$), 1-methyl-3-propylimidiazolium iodide (PMII) ≥ 98%, tetrabutylammonium iodide (TBAI) ≥ 98, 3,4-ethylenedioxythiophene (EDOT) 97%, titanium(IV) isopropoxide ($Ti(OiPr)_4$), Alconox, and solvents (anhydrous acetonitrile (ACN) 99.8%, ACS grade 2-propanol ≥ 99.8%, 99.9% 1-butanol and anhydrous methanol 99.8%) were purchased from Merck and used without further purification. Ultra dry LiI 99.999% and Magnesium iodide (MgI_2) > 99% were obtained from Fluka. $LiClO_4$ ≥ 99% was purchased from Acros organics. 1-Methyl-3-propylimidiazolium trifluoromethanesulfonate (PMIOTf) was bought from Tokyo Chemical Industry (TCI). FTO TEC-7 was purchased from NSG. Surlyn 25, Ti-nanoxideT/SP and Ti-nanoxide R/SP pastes were obtained from Solaronix.

Photoanodes preparation

The Fluorine Thin Oxide (FTO) slides underwent sequential cleaning by immersion and ultrasonic treatment: first in a 1% Alconox solution, then in 2-propanol, each for 10 min. The process was followed by annealing for 20 min at 450 °C. A compact blocking underlayer was generated by spin coating a 0.3 M Ti(IV)$(OiPr)_4$/1-butanol solution (10 s at 1000 rpm and 20 s at 2000 rpm), then sintered at 500 °C for 15 min. The mesoporous TiO_2 active layer was deposited by doctor blading between to two 3 M tape slides set at 5 mm of distance. The

sintering protocol involved heating from RT to 120 °C at 10 °C min^{-1}, from 120 °C to 450 °C at 11 °C min^{-1}, rest at 450 °C for 30 min, ramp step to 500 °C at 5 °C min^{-1} and rest at 10 min at 500 °C. This preparation of the mesoporous titania film was repeated up to 3 times to achieve greater thickness. Final treatment with TiCl was performed by drop casting followed by slow hydrolysis using a 0.4 M TiCl/water solution in a sealed chamber for 12 h at room temperature. Resulting films were washed with deionized water, dried with an air flux and annealed for 30 min at 450 °C. The scattering top layer was produced with the same protocol as the active TiO_2 film but employing a reflective paste (Ti-nanoxide R/SP, Solaronix) and identical sintering conditions.

Sensitizer molecules were absorbed onto TiO_2 electrodes from a 0.2 mM dye/0.04 mM chenodeoxycholic (CDCA) acetonitrile solution.

DSSC fabrication

PEDOT-based counter electrodes were prepared by electropolymerizing a mixture of 10^{-2} EDOT and 10^{-1} M $LiClO_4$ in ACN, by means of Cyclic Voltammetry. Potential was scanned from 0 to 1.6 V *vs.* SCE at 50 mV s^{-1}, with a cleaned FTO slide as the working electrode assembled face-to-face 2.3 mm from a titanium sheet (A = 4 cm^2) as counter electrode, and a double jacket SCE as reference.

Device assembly involved open configuration cells in which the electrolyte was confined within a delimited region using Surlyn 25 thermoplastic spacer. Photoanode and counterelectrode were held together by two clamps. Cells were filled with our customized electrolyte consisting of 0.1 M LiI, 0.6 M PMII, 0.1 M I_2, 0.1 MgI_2, 0.1 M GuNCS, 0.1 M TBAI in acetonitrile.

Spectroscopic and electrochemical methods and data

Absorption spectra of the Fe(II)NHC sensitized photoanodes were measured in transmission mode with an Agilent Carry 300 UV-Vis spectrophotometer, an undyed TiO_2 electrode as a reference. For opaque substrates, spectra were acquired in diffuse reflectance mode with a JASCO V-570 spectrophotometer an integrating sphere, illuminating through the FTO side. Spectra are reported in Kubelka–Munk (KM) units.

Fourier transform infrared-attenuated total reflection spectroscopy (FTIR-ATR) of the sensitized TiO_2 was performed with a Nicolet iS50 spectrometer with a 45° single-reflection diamond ATR element. A total of 32 scans were averaged for each spectrum.

Titania or zirconia layers functionalized with the Fe(II)NHC complexes were used as working electrodes for cyclic voltammetry (CV), in a three-electrode cell with a platinum wire as counter-electrode and a Saturated Calomel Electrode (SCE) as reference. Measurements were recorded with a PGSTAT 302N potentiostat at a scan rate of 50 mV s^{-1} in 0.1 M $LiClO_4$/ACN solution.

Photocurrent density–voltage (JV) curves were obtained using a PGSTAT 302N potentiostat coupled with an ABET solar simulator and an AM1.5G filter, with incident light power set to 100 mW cm^{-2} (1 SUN). Incident-Photon-to-Current-Conversion Efficiency (IPCE%) spectra were collected using a custom setup with a Xenon lamp (Ceralux CL300BF) and a National Instrument PXI 1033, under short circuit conditions. Absorbed Photon to Current Conversion Efficiency (APCE%) spectra were computed *via* APCE% = IPCE%/LHE (Light Harvesting Efficiency), where LHE was derived from absorption spectra using LHE = $1–10^{-A(\lambda)}$.

Transient Absorption Spectroscopy (TAS) of the Fe(II)NHC sensitized TiO_2 films was performed using a Nd:YAG laser (Continuum Surelite II) and monochromatic probe beam, holding the FTO slides at 45° to both beams to divert stray light away from the photomultiplier tube (PMT). Signal-to-noise-ratio (S/N) was improved by averaging *ca.* 50 laser shots, with pre-amplification adjusted between 350 Ω to 1 M Ω depending on the experimental timescale. Fe(II)NHC sensitized films were exposed to 0.1 M $LiClO_4$/ACN solution or with a blank electrolyte (deprived of I^- and I_2) (0.1 M LiOTf, 0.6 M PMIOTf, 0.1 M GuNCS, 0.1 M $TBAPF_6$, 0.1 $MgOTf_2$) or a reduced form of the electrolyte (without I_2) (0.1 M LiI, 0.6 M PMII, 0.1 MgI_2, 0.1 M GuNCS, 0.1 M TBAI). The contact between dyed film and electrolyte was achieved by pressing a glass slide onto the sensitized surface and filling the void by capillarity with the appropriate solution.

Ab initio calculations

All the quantum chemical calculations presented in this work were carried out in the Density Functional Theory (DFT) framework using the Gaussian 16 software package (Revision C.01).[37] Geometry optimizations in the ground state ($^1S_0$) were performed without symmetry constraints using the B3LYP* hybrid density functional[38,39] in combination with the triple-zeta Pople-type Gaussian basis set (6-311G(d,p)). The B3LYP* functional, in which the percentage of Hartree–Fock exchange is decreased to 15% from 20% (as in the standard B3LYP) has been shown to provide an improved description of the electronic structure and spin-state energetics of first-row transition metal complexes, especially Fe(II) complexes.[40–45] For the complex **NS252**, characterized by a higher degree of electron delocalization and CT, the standard B3LYP functional was employed. Vibrational frequency calculations (infrared and Raman) were carried out at the same level of theory to confirm the optimized geometries as true minima on the potential energy surface (no imaginary frequencies). Solvent effects were accounted by means of conductor-like polarizable continuum model (C-PCM),[46–48] with acetonitrile (CH_3CN) as the solvent (ε = 37.5).

Vertical excitation energies were calculated within time-dependent density functional theory in the linear response regime (LR-TD-DFT) using the same level of theory adopted for geometry optimizations. For each system, the lowest 50 singlet excited states were computed to characterize the UV-Vis spectrum. Natural transition orbitals (NTO) analysis[49] of the low-lying bright excited states was performed to obtain a more concise and chemical intuitive representation of the excited states. TheoDORE package[50] was employed to analyse the transition density matrix, providing detailed information on the

nature and composition of the electronic transitions, as well as the spatial distribution of the excitation density across the different fragments of the complexes.

Conclusions

A family of Fe(II) sensitizers incorporating pyridyl–NHC ligands extended with fused thiophenes of variable number has been prepared with the aim of enhancing the light-harvesting window of iron-sensitized solar cells (FeSSCs). The complexes have been thoroughly characterized in both solution and anchored to TiO_2 photoanodes by means of electrochemistry, transient absorption spectroscopy, and *ab initio* calculations. Upon photoexcitation, charge injection into TiO_2 was observed, leading to long-lived charge-separated states capable of interacting with the redox mediator with nearly quantitative efficiency.

Within the series, **NS252**, which bears both a thienylcyanoacrylic anchoring group and a fused dithienyl moiety, exhibited the broadest spectral response, enabling photon collection up to 750 nm. Although this sensitizer also displayed the lowest IPCE (25%), it demonstrates the potential of structural changes to further expand the absorption window. The best device performance was achieved with **ARM15**, bearing a single thiophene unit, which delivered an efficiency of 1.5% and a photocurrent of 6.46 mA cm^{-2} when chemisorbed on an 18 μm thick photoanode. More π-extended systems-maintained efficiencies close to 1%, underscoring their promise. The reduced performance in these new systems is attributed to charge density localization on fused thiophenes positioned opposite to the anchoring units, limiting the electron injection efficiency into the TiO_2. This work highlights a critical challenge in the design of efficient Fe(II) sensitizers for DSSCs: the need to balance sufficiently long-lived excited-state lifetimes, a broad light-harvesting window, and effective excited-state directionality for charge injection.

Author contributions

N. S. prepared the complexes and characterized them in their ground state. E. M. an R. A. assembled the DSSCs performed photoelectrochemistry, transient spectroscopy and analysed the data with S. C., F. C. and M. P. performed the computational analysis. P. P. and P. C. G. conceived the project and wrote the paper with E. M., S. C. and M. P.

Conflicts of interest

There are no conflicts to declare.

Data availability

The data supporting this article have been included as part of the supplementary information (SI). Supplementary information is available. See DOI: https://doi.org/10.1039/d5dt02301g.

Acknowledgements

N. S. gratefully acknowledges the University of Lorraine for PhD grant. The L2CM thanks the mass spectrometry MassLor platform (L2CM & LCPA2MC, University of Lorraine) and the CPM NMR facility (CRM2, University of Lorraine). S. C. acknowledges financial support from PNRR MUR project ECS_00000033_ECOSISTER. E. M. acknowledges financial support from PRIN MUR project "SUN-SPOT" (Prot. 2022JA3PSC). M. P. acknowledges HPC resources from MESOCENTRE EXPLOR of the University of Lorraine (project 2018CPMXX0602). In memory of Pr Carlo Alberto Bignozzi.

References

1 T. Duchanois, L. Liu, M. Pastore, A. Monari, C. Cebrián, Y. Trolez, M. Darari, K. Magra, A. Francés-Monerris, E. Domenichini, M. Beley, X. Assfeld, S. Haacke and P. Gros, *Inorganics*, 2018, **6**, 63.
2 O. S. Wenger, *J. Am. Chem. Soc.*, 2018, **140**, 13522–13533.
3 S. Kaufhold and K. Wärnmark, *Catalysts*, 2020, **10**, 132.
4 P. Dierks, Y. Vukadinovic and M. Bauer, *Inorg. Chem. Front.*, 2022, **9**, 206–220.
5 J. R. Durrant, S. A. Haque and E. Palomares, *Coord. Chem. Rev.*, 2004, **248**, 1247–1257.
6 A. Listorti, C. Creager, P. Sommeling, J. Kroon, E. Palomares, A. Fornelli, B. Breen, P. R. F. Barnes, J. R. Durrant, C. Law and B. O'Regan, *Energy Environ. Sci.*, 2011, **4**, 3494.
7 A. Listorti, B. O'Regan and J. R. Durrant, *Chem. Mater.*, 2011, **23**, 3381–3399.
8 F. Perrella, X. Li, A. Petrone and N. Rega, *JACS Au*, 2023, **3**, 70–79.
9 L. Liu, T. Duchanois, T. Etienne, A. Monari, M. Beley, X. Assfeld, S. Haacke and P. C. Gros, *Phys. Chem. Chem. Phys.*, 2016, **18**, 12550–12556.
10 Y. Liu, T. Harlang, S. E. Canton, P. Chábera, K. Suárez-Alcántara, A. Fleckhaus, D. A. Vithanage, E. Göransson, A. Corani, R. Lomoth, V. Sundström and K. Wärnmark, *Chem. Commun.*, 2013, **49**, 6412.
11 M. Darari, E. Domenichini, A. Francés-Monerris, C. Cebrián, K. Magra, M. Beley, M. Pastore, A. Monari, X. Assfeld, S. Haacke and P. C. Gros, *Dalton Trans.*, 2019, **48**, 10915–10926.
12 K. Magra, E. Domenichini, A. Francés-Monerris, C. Cebrián, M. Beley, M. Darari, M. Pastore, A. Monari, X. Assfeld, S. Haacke and P. C. Gros, *Inorg. Chem.*, 2019, **58**, 5069–5081.
13 K. Magra, A. Francés-Monerris, C. Cebrián, A. Monari, S. Haacke and P. C. Gros, *Eur. J. Inorg. Chem.*, 2022, **2022**, e202100818.

14 K. Magra, M. Darari, E. Domenichini, A. Francés-Monerris, C. Cebrián, M. Beley, M. Pastore, A. Monari, X. Assfeld, S. Haacke and P. C. Gros, *J. Phys. Chem. C*, 2020, **124**, 18379–18389.
15 E. Marchini, M. Darari, L. Lazzarin, R. Boaretto, R. Argazzi, C. A. Bignozzi, P. C. Gros and S. Caramori, *Chem. Commun.*, 2020, **56**, 543–546.
16 A. Reddy-Marri, E. Marchini, V. D. Cabanes, R. Argazzi, M. Pastore, S. Caramori and P. C. Gros, *J. Mater. Chem. A*, 2021, **9**, 3540–3554.
17 M. Becker, C. E. Housecroft and E. C. Constable, *Materials*, 2021, **14**, 3053.
18 M. Becker, V. Wyss, C. E. Housecroft and E. C. Constable, *Dalton Trans.*, 2021, **50**, 16961–16969.
19 L. Lindh, O. Gordivska, S. Persson, H. Michaels, H. Fan, P. Chábera, N. W. Rosemann, A. K. Gupta, I. Benesperi, J. Uhlig, O. Prakash, E. Sheibani, K. S. Kjaer, G. Boschloo, A. Yartsev, M. Freitag, R. Lomoth, P. Persson and K. Wärnmark, *Chem. Sci.*, 2021, **12**, 16035–16053.
20 A. Reddy-Marri, E. Marchini, V. D. Cabanes, R. Argazzi, M. Pastore, S. Caramori, C. A. Bignozzi and P. C. Gros, *Chem. – Eur. J.*, 2021, **27**, 16260–16269.
21 A. Reddy-Marri, E. Marchini, V. D. Cabanes, R. Argazzi, M. Pastore, S. Caramori and P. C. Gros, *Chem. Sci.*, 2023, **14**, 4288–4301.
22 M. Pastore, S. Caramori and P. C. Gros, *Acc. Chem. Res.*, 2024, **57**, 439–449.
23 S. Mukherjee, D. E. Torres and E. Jakubikova, *Chem. Sci.*, 2017, **8**, 8115–8126.
24 J. D. Braun, I. B. Lozada and D. E. Herbert, *Inorg. Chem.*, 2020, **59**, 17746–17757.
25 J. D. Braun, I. B. Lozada, C. Kolodziej, C. Burda, K. M. E. Newman, J. van Lierop, R. L. Davis and D. E. Herbert, *Nat. Chem.*, 2019, **11**, 1144–1150.
26 A. R. Marri, B. Marekha, T. Penfold, S. Haacke and P. C. Gros, *Inorg. Chem. Front.*, 2023, **10**, 118–126.
27 T. Duchanois, T. Etienne, C. Cebrián, L. Liu, A. Monari, M. Beley, X. Assfeld, S. Haacke and P. C. Gros, *Eur. J. Inorg. Chem.*, 2015, **2015**, 2469–2477.
28 Y. Tachibana, J. E. Moser, M. Grätzel, D. R. Klug and J. R. Durrant, *J. Phys. Chem.*, 1996, **100**, 20056–20062.
29 S. E. Koops, B. C. O'Regan, P. R. F. Barnes and J. R. Durrant, *J. Am. Chem. Soc.*, 2009, **131**, 4808–4818.
30 T. D. Santos, A. Morandeira, S. Koops, A. J. Mozer, G. Tsekouras, Y. Dong, P. Wagner, G. Wallace, J. C. Earles, K. C. Gordon, D. Officer and J. R. Durrant, *J. Phys. Chem. C*, 2010, **114**, 3276–3279.
31 A. Hagfeldt, G. Boschloo, L. Sun, L. Kloo and H. Pettersson, *Chem. Rev.*, 2010, **110**, 6595–6663.
32 J. R. Durrant, S. A. Haque and E. Palomares, *Coord. Chem. Rev.*, 2004, **248**, 1247–1257.
33 A. Y. Anderson, P. R. F. Barnes, J. R. Durrant and B. C. O'Regan, *J. Phys. Chem. C*, 2011, **115**, 2439–2447.
34 P. K. Nayak, G. Garcia-Belmonte, A. Kahn, J. Bisquert and D. Cahen, *Energy Environ. Sci.*, 2012, **5**, 6022–6039.
35 R. García-Rodríguez, J. Villanueva-Cab, J. Anta and G. Oskam, *Materials*, 2016, **9**, 33.
36 A. J. Bard and L. R. Faulkner, *Electrochemical Methods, Fundamentals and Applications*, John Wiley & Sons, New York, NY, 2nd edn, 2001.
37 M. J. Frisch, G. W. Trucks, H. B. Schlegel, G. E. Scuseria, M. A. Robb, J. R. Cheeseman, G. Scalmani, V. Barone, G. A. Petersson, H. Nakatsuji, X. Li, M. Caricato, A. V. Marenich, J. Bloino, B. G. Janesko, R. Gomperts, B. Mennucci, H. P. Hratchian, J. V. Ortiz, A. F. Izmaylov, J. L. Sonnenberg, D. Williams-Young, F. Ding, F. Lipparini, F. Egidi, J. Goings, B. Peng, A. Petrone, T. Henderson, D. Ranasinghe, V. G. Zakrzewski, J. Gao, N. Rega, G. Zheng, W. Liang, M. Hada, M. Ehara, K. Toyota, R. Fukuda, J. Hasegawa, M. Ishida, T. Nakajima, Y. Honda, O. Kitao, H. Nakai, T. Vreven, K. Throssell, J. A. Montgomery Jr., J. E. Peralta, F. Ogliaro, M. J. Bearpark, J. J. Heyd, E. N. Brothers, K. N. Kudin, V. N. Staroverov, T. A. Keith, R. Kobayashi, J. Normand, K. Raghavachari, A. P. Rendell, J. C. Burant, S. S. Iyengar, J. Tomasi, M. Cossi, J. M. Millam, M. Klene, C. Adamo, R. Cammi, J. W. Ochterski, R. L. Martin, K. Morokuma, O. Farkas, J. B. Foresman, and D. J. Fox, *Gaussian 16, Revision C.01*, Gaussian, Inc., Wallingford CT, 2016.
38 M. Reiher, *Inorg. Chem.*, 2002, **41**, 6928–6935.
39 O. Salomon, M. Reiher and B. A. Hess, *J. Chem. Phys.*, 2002, **117**, 4729–4737.
40 M. Reiher, O. Salomon and B. A. Hess, *Theor. Chem. Acc.*, 2001, **107**, 48–55.
41 L. A. Fredin, M. Pápai, E. Rozsályi, G. Vankó, K. Wärnmark, V. Sundström and P. Persson, *J. Phys. Chem. Lett.*, 2014, **5**, 2066–2071.
42 I. M. Dixon, F. Alary, M. Boggio-Pasqua and J.-L. Heully, *Dalton Trans.*, 2015, **44**, 13498–13503.
43 K. P. Kepp, *Inorg. Chem.*, 2016, **55**, 2717–2727.
44 A. Francés-Monerris, P. C. Gros, M. Pastore, X. Assfeld and A. Monari, *Theor. Chem. Acc.*, 2019, **138**, 86.
45 A. Francés-Monerris, P. C. Gros, X. Assfeld, A. Monari and M. Pastore, *ChemPhotoChem*, 2019, **3**, 666–683.
46 J. Tomasi, B. Mennucci and R. Cammi, *Chem. Rev.*, 2005, **105**, 2999–3094.
47 V. Barone and M. Cossi, *J. Phys. Chem. A*, 1998, **102**, 1995–2001.
48 M. Cossi, N. Rega, G. Scalmani and V. Barone, *J. Comput. Chem.*, 2003, **24**, 669–681.
49 R. L. Martin, *J. Chem. Phys.*, 2003, **118**, 4775–4777.
50 F. Plasser, *J. Chem. Phys.*, 2020, **152**, 084108.